



Cryo-EM structure of the human histamine H₁ receptor/G_q complex

Ruixue Xia^{1,3}, Na Wang^{1,3}, Zhenmei Xu^{1,3}, Yang Lu¹, Jing Song¹, Anqi Zhang², Changyou Guo² & Yuanzheng He¹  

Histamine receptors play important roles in various pathophysiological conditions and are effective targets for anti-allergy treatment, however the mechanism of receptor activation remain elusive. Here, we present the cryo-electron microscopy (cryo-EM) structure of the human H₁R in complex with a G_q protein in an active conformation via a NanoBiT tethering strategy. The structure reveals that histamine activates receptor via interacting with the key residues of both transmembrane domain 3 (TM3) and TM6 to squash the binding pocket on the extracellular side and to open the cavity on the intracellular side for G_q engagement in a model of “squash to activate and expand to deactivate”. The structure also reveals features for G_q coupling, including the interaction between intracellular loop 2 (ICL2) and the αN-β junction of G_{q/11} protein. The detailed analysis of our structure will provide a framework for understanding G-protein coupling selectivity and clues for designing novel antihistamines.

¹Laboratory of Receptor Structure and Signaling, The HIT Center for Life Sciences, Harbin Institute of Technology, Harbin, China. ²The HIT cryo-EM facility, Harbin Institute of Technology, Harbin, China. ³These authors contributed equally: Ruixue Xia, Na Wang, Zhenmei Xu. ✉email: ajian.he@hit.edu.cn

Histamine is a biogenic amine that mediates a variety of pathophysiological responses and signaling events through the binding of histamine receptors, members of the class A G-protein-coupled receptor (GPCR) superfamily¹. There are four types of histamine receptors, H₁R, H₂R, H₃R, and H₄R². H₁R and H₂R are validated targets for the treatment of allergies and forms of gastric acid-related conditions, while H₃R and H₄R have a clinical potential for dementia, asthma, inflammatory bowel disease, and rheumatoid arthritis^{1,3–5}. Histamine binding of receptor recruits heterotrimeric G-protein and triggers downstream signaling cascade. The H₁R is mainly coupled with G_q protein that activates phospholipase C to increase inositol phosphates and intracellular calcium level, H₂R couples to G_s protein to stimulate cAMP production, H₃R and H₄R signals through G_{i/o} proteins².

Histamine has an active role in allergy and anaphylaxis and is mainly mediated by H₁R³. The earliest use of antihistamines for allergic disorders can be traced back to early 1950s and over more than half century antihistamines remain as the first choice for many allergic disorders, such as allergic rhinitis, hay fever, and urticaria³. Early antihistamines can easily penetrate the blood-brain barrier and have low receptor selectivity, therefore have considerable side effects such as sedation, dry mouth, and arrhythmia^{6,7}. The later introduction of carboxyl moiety and protonated amine improve receptor selectivity and significantly reduce side effects associated with brain permeability. However, even the second- or third-generation antihistamine, such as Certirizine (Zyrtec), Loratidine (Claritin), and Fexofenadine (Allegra) still have some unwanted side effects, such as drowsiness, dizziness, and headache^{1,8,9}. The most successful antihistamine design is bulky molecules with a basic amino group which is very different from the simple imidazole ring and ethylamine side chain of histamine³, yet the mechanism by which those bulky antihistamines block the H₁R signaling is still unknown.

An early study has revealed the structure of H₁R bound to the first generation of antihistamine, doxepin, in an inactive conformation¹⁰. The structure revealed that the amine moiety of doxepin forms a salt bridge with a strictly conserved D107^{3,32} and the bulky tricyclic dibenzoxepin ring sets in a hydrophobic pocket formed by conserved residues of TM 3, 5 and 6. The study also explained the improvement of specificity of the second generation of antihistamine via the docking method. However, lacking the active conformation of the receptor, the paper did not articulate a clear mechanism by which those inverse agonists inactivate receptor. Limited structural information of the receptor, particularly the lack of precise agonist binding information and the active conformation of receptor, hampered the development of novel antihistamine that may shut down the receptor activity more effectively and have less side effects.

GPCRs primarily couple to 4 major G α families, G_s, G_{i/o}, G_{q/11}, and G_{12/13}, that dictate different signaling cascade¹¹. Considering the large number of receptors (more than 800) and the limited number of G protein (16 of 4 families)¹², a general question is whether there is a selective barcode for receptor/G-protein recognition. A number of studies have suggested that the engagement of G-protein to receptor is more complicated than previously envisioned^{13–15}, and there is no simple primary or second structural pattern on receptor/G-protein recognition. A barcode, if exists, it must lie in the tertiary or even the quaternary structure of receptor/G-proteins complex. A number of GPCR/G_s and GPCR/G_i complexes have been solved by cryo-EM, however, there is very few of G_{q/11}-coupled receptor complex structure available. The muscarinic acetylcholine receptor 1 (M1R)/G₁₁ complex structure first revealed some distinct features for the G_{q/11}-coupled receptors, including an extended TM5 and a receptor

c-tail/G-protein interaction¹⁶. Most recently, a 5-HT_{2A} serotonin receptor (HTR2A)/mini-G_q protein complex structure was solved¹⁷. It is imaginable that with more G_q-coupled receptor complex structures being solved, a pattern of receptor/G_q engagement can be found.

Here, we present a cryo-EM structure of H₁R in complex with a N-terminal engineered G_q protein by a NanoBiT tethering strategy. The structure reveals the mechanism of ligand-induced receptor activation in a model of “squash to activate and expand to deactivate” (Supplementary Fig. 1). Our structure analysis also unravels some distinct features of H₁R/G_q engagement. These findings could help to understand the G_q coupling selectivity and provide clues for designing novel antihistamines that can more specifically block histamine signaling and have fewer side effects.

Results

The overall structure of H₁R/G_q complex. To facilitate the cryo-EM structure solving, we use an engineered G_q protein (G_{qIN}) in which the N-terminus (residue 1–32) of G_q was replaced by the N-terminus (residue 1–28) of G_i protein to render the protein binding ability to the scFv16 antibody that has been successfully used in solving numerous receptor/G-protein complexes^{16,18–20}, including the M1R/G₁₁ complex. Also the long ICL3 of H₁R (residue 224–401) was deleted to improve protein expression and folding. The initial attempt to get a stable complex via co-expression of the receptor, G_{qIN} and scFV16 was not very successful. We then adopted the NanoBiT tethering strategy²¹ in which the C-terminus of H₁R was fused to the large part of NanoBiT (LgBiT), and the C-terminus of G β was fused to the renovated 13-amino acid peptide of NanoBiT (HiBiT) (Supplementary Fig. 2). This strategy has been successfully used in solving several GPCR/G-protein complexes structures, including the vasoactive intestinal polypeptide receptor²¹ (VIP1R)/G_s and growth hormone-releasing hormone receptor/G_s complexes²². Indeed, the NanoBiT tethering strategy greatly improves the composition of the complex (Supplementary Fig. 3), and the structure was solved by the single-particle cryo-EM analysis of the H₁R-LgBiT/G_{qIN}/G β -HiBiT/G γ /scFv16 complex at 3.64 Å resolution (Methods and Supplementary Figs. 4–6). The overall reconstruction of the H₁R/G_q complex is shown in Fig. 1a with the resulting model in Fig. 1b. The global arrangement of the complex is similar to other GPCR/G-protein complexes with the G α protein engaging with the intracellular side of the receptor. Local resolution analysis shows that the WD40 repeat domain of G β and the core transmembrane domain of the receptor have the highest resolution, the extracellular part of receptor, the border of G α RAS domain and the N-terminus of G $\beta\gamma$ have the relative lower resolution (Supplementary Fig. 5a). The alpha helical domain of G α cannot be resolved in our analysis due to its high flexibility. We also observed trace amount of density of the NanoBiT complex formed by the LgBiT and HiBiT (Supplementary Fig. 7), however, the local resolution much worse than 6 Å, we therefore omit it in the later structural analysis. Previous VIP1R study has shown that the fusion of LgBiT to receptor has almost no effect on the function of the receptor. We also did a nuclear factor of activated T-cells response element (NFAT-RE) reporter assay, a well-established reporter assay for the G_{q/11} signaling pathway²³, showing that the fusion of LgBiT to H₁R only marginally affects receptor activity (Supplementary Fig. 2c). Because of the NanoBiT density is far from the receptor/G_q interface (Supplementary Fig. 7) and the fusion of LgBiT do not affect receptor's response to histamine, we reason that the complex structure of H₁R-LgBiT/G_{qIN}/G β -HiBiT/G γ represents the complex structure of H₁R/G_q, and hence use H₁R/G_q to represent the complex in this study. The transmembrane helical bundle has

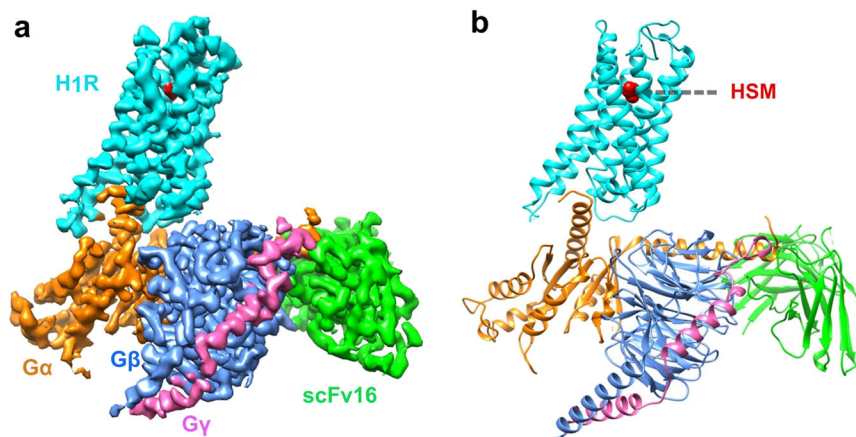


Fig. 1 Overall structure of the H₁R/G_q complex. **a** Orthogonal views of the cryo-EM density map of the H₁R/G_q complex. **b** Model of the complex in same view and color scheme as shown in **(a)**. HSM: histamine.

strong electron signal and the histamine ligand is well resolved in the ligand-binding pocket (discussed in detail in the following section).

Histamine binding and the ligand-binding pocket. The native ligand histamine is well resolved in the ligand-binding pocket (Fig. 2a). The structure shows that all three histamine nitrogen atoms establish hydrogen bonds with the surrounding polar residues from TM3, TM5, and TM6. The primary amino group of histamine (N^α) forms hydrogen bonds with the D107^{3.32} of TM3 and Y431^{6.51} of TM6, the 1 position nitrogen atom (N^η) of the imidazole ring form a hydrogen bond with Y431^{6.51} of TM6, and the 3 position nitrogen atom (N^γ) forms hydrogen bonds with N198^{5.46} of TM5 and T112^{3.37} of TM3 (Fig. 2a). Those key positions are conserved in the histamine receptor family (Supplementary Fig. 8) and the interactions are confirmed by mutation experiment on the NFAT-RE reporter assay. Single mutation of D107A, N198A, and Y431F totally abolish histamine-induced receptor activation (Fig. 2b), suggesting that they play a key role in ligand binding. The T112A mutation only partially decreases the ligand-induced receptor activity, this may be due to the factor that the N^γ atom also forms hydrogen bond with the N198^{5.46} of TM5. On the other hand, the Y108F and S111A mutations do not have a detrimental effect on ligand-induced receptor activation, indicating that they do not participate the forming of the hydrogen bond network with the ligand. Interestingly those two residues are also not conserved in the histamine receptor family (Supplementary Fig. 8). The periphery of the ligand-binding pocket is surrounded by hydrophobic residues, including W428^{6.48}, F432^{6.52}, F435^{6.55}, and W158^{4.56} (Fig. 2a). To investigate whether those non-polar bulky residues also contribute to receptor activation through hydrophobic or van der Waals interactions, we mutate those bulky residues (including two polar bulky residues that do not form hydrogen bond with histamine, Y108^{3.33} and Y458^{7.43}) to small non-polar residues and test them in the NFAT-RE reporter assay. The data show that mutation of W158A and W428A totally abolish receptor activation, and F435A severely affects receptor activity (Supplementary Fig. 9), suggesting that they may play a crucial role in defining the ligand-binding pocket and providing some necessary hydrophobic interaction to support the correct ligand binding. Particularly, the W428^{6.48} of the conserved CWxP motif is the “toggle-switch” of receptor, plays a key role in switching receptor from inactive state to active state. The Y108V and Y458A mutations retain about half of receptor activity, and the F432A and I454A mutations are almost as active as the wild-type receptor, suggesting those

residues do not directly participate ligand binding. An electrostatic potential calculated and analyzed by the APBS Electrostatics PyMol Plugin shows a negative charged pocket setting on the up-middle (toward the extracellular side) of the receptor (Fig. 2c). The pocket is formed by D107^{3.32}, Y458^{7.43}, Y431^{6.51}, N198^{5.46}, T112^{3.37}, Y108^{3.33}, S111^{3.36}, and histamine sets right middle of the pocket.

Active H₁R vs inactive H₁R. Compared to the inactive conformation of doxepin-bound H₁R¹⁰ (C α root-mean-square deviation of 1.235 Å), the biggest difference is the squash of ligand-binding pocket in the active conformation. Calculating by the CASTp 3.0 server²⁴, the solvent-accessible volume of doxepin-bound H₁R is 249 Å³, and the histamine-bound H₁R is 79 Å³ (Supplementary Fig. 10). A close look at the ligand-binding sites shows that in the active conformation, the agonist histamine forms hydrogen bonds with D107^{3.32}, T112^{3.37} of TM3 on one side, and forms hydrogen bond with the Y431^{6.51} of TM6 on the other side, acting as a magnet to pull the extracellular half of TM6 toward TM3 (Fig. 3a). Although the inverse agonist doxepin also forms hydrogen bond with the conserved D107^{3.32} of TM3, its hydrophobic tricyclic dibenzooxepin ring cannot form a hydrogen bond with Y431^{6.51} of TM6, in fact the bulky tricyclic dibenzooxepin ring push F432^{6.52} and F435^{6.55} of TM6 away from TM3 (Fig. 3b). It is conceivable that the contraction of the extracellular binding pocket can lead to the expansion of the intracellular end, thus to open the hydrophobic cavity of the intracellular side for transducer engagement, as seen in β 2 adrenergic receptor (β 2-AR)/G_s, M1R/G₁₁ and cannabinoid receptor 1 (CB1)/G_i complex^{16,25,26}. Indeed, we see an inward displacement of the extracellular part of TM6 (2.6 Å measured by the C α of A439^{6.59}) and a dramatic outward displacement of the intracellular part of TM6 (11.6 Å as measured by the C α of N408^{6.28}) upon ligand binding (Fig. 3a). The conserved W428^{6.48} serves as a pivot point for these movements, where the “up” (extracellular) side move inward (4.6 degree), and the “down” (intracellular) side move outward (20.5 degree) (Fig. 3c). We also see the coordinated movements of TM3, TM2, and TM7 in squashing the binding pocket and opening the hydrophobic cavity of the intracellular side (Fig. 3a). Together, those movements render receptor in an active conformation, enabling the engagement of the α H5 of G α_q . Based on those observations, we postulate that the key mechanism for receptor activation is to squash the ligand-binding pocket via the hydrogen bonds formed by histamine with key residues of TM3 and TM6. To test the hypothesis, we have mutated the Y431^{6.51}, the key residue of TM6 that forms hydrogen bond with

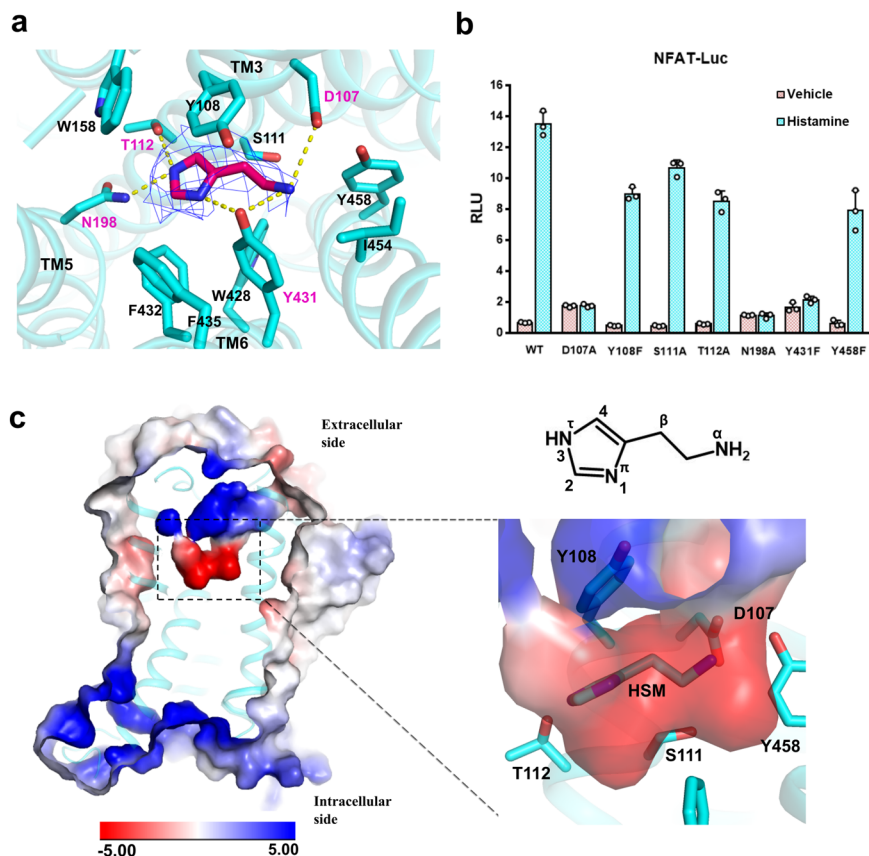


Fig. 2 Histamine binding and the ligand-binding pocket. **a** The ligand-binding pocket of histamine. The histamine is shown in red in the middle of the pocket, density map of histamine (blue mesh) is set at contour level of 3.0. Surrounding residues within 4.1 Å of histamine are shown in sticks and colored in cyan. Hydrogen bonds are marked as yellow dash line. **b** A NFAT-RE reporter assay of mutations of key residues in the ligand-binding pocket. Histamine, 10 μM; data are presented as mean values ± SD; *n* = 3 independent samples. RLU, relative luciferase unit. WT, wild-type. **c** The electrostatic potential surface of H₁R and the histamine binding pocket. The chemical structure of histamine is shown on the up-right panel.

the N^π of histamine, to the positive charged residue R, rendering it ability to form a salt bridge with the negative charged residue D107^{3,32} to mimic the effect of histamine to pull TM6 toward TM3 (Fig. 3d). In the NFAT-RE reporter assay, the Y431R shows high basal activity (Fig. 3e). To prove the high basal activity is caused by the salt bridge interaction, we mutated D107^{3,32} to N. The data show that the combination of Y431R/D107N or D107N alone has almost no basal activity. To further prove the lost basal activity of the Y431R/D107N is due to the loss of salt-bridge interaction, we also mutate D107^{3,32} to E which retains the ability to form a salt bridge with Y431R. The data shows while D107E has no basal activity as the D107N, the combination of Y431R/D107E retains the most basal activity of Y131R (Fig. 3e), suggesting the high basal activity indeed comes from the salt-bridge interaction between TM3 and TM6. We also obtained similar results when Y431^{6,51} is mutated to K (Supplementary Fig. 11). Taken together, we propose a model of “squash to activate and expand to deactivate” for H₁R action (Supplementary Fig. 1) where agonist activates receptor via forming hydrogen bonds with TM3 and TM6 to squash ligand-binding pocket on the extracellular side and open the cavity for G-protein engagement on the intracellular side; on the other hand, antihistamine (inverse agonist) use its bulky group to expand the ligand-binding pocket on the extracellular side and to close the G-protein binding cavity on the intracellular side to shut down receptor signaling. Indeed, a comparison of doxepin-bound H₁R with histamine-bound H₁R shows that the bulky tricyclic dibenzooxepin ring of doxepin pushes F432^{6,52} and F435^{6,55} of TM6 away from TM3. It is also

very interesting to find that the most successful antihistamines are those with bulky ring group, such as fexofenadine (Allergra), loratadine (Claritin), and cetirizine (Zyrtec) (Supplementary Fig. 12), further supporting the idea of “expand to deactivate and squash to activate”. To examine whether this is a specific activation mechanism for H₁R, or it is common mechanism for monoamine GPCRs, we compared the size of agonist and antagonist binding pockets of H₁R with β₂-AR, dopamine receptor DRD2 and serotonin receptor HTR2A, members of the monoamine GPCRs (Supplementary Fig. 13). The side-by-side comparisons show that the ligand-binding pocket of H₁R condenses most dramatically upon agonist binding, the β₂-AR ligand-binding pocket slightly shrinks while there is no significant change in the size of DRD2 pocket upon agonist binding, and HTR2A’s pocket actually increase upon agonist binding. Those data suggest that the “squash to activate and expand to deactivate” might be a more specific model for H₁R action.

We also look at how the activation signal on the extracellular side is transmitted to the intracellular side via examining the conformational changes on the conserved DRY, CWxP, NPxxY, and PIF motifs. Those motifs lie on the intracellular half of receptor and are usually associated with locking receptor in the inactive state (Supplementary Fig. 14). The CWxP motif of TM3 lies in the hinge region of receptor where the extracellular side signal is transmitted to the intracellular side of receptor. In receptor activation, the binding of agonist ligand histamine triggers the rotameric switch of W428^{6,48} and the concomitant side chain rotation of Y431^{6,51}, F432^{6,52}, F424^{6,44} and F199^{5,47}, initiating the rotation of TM6.

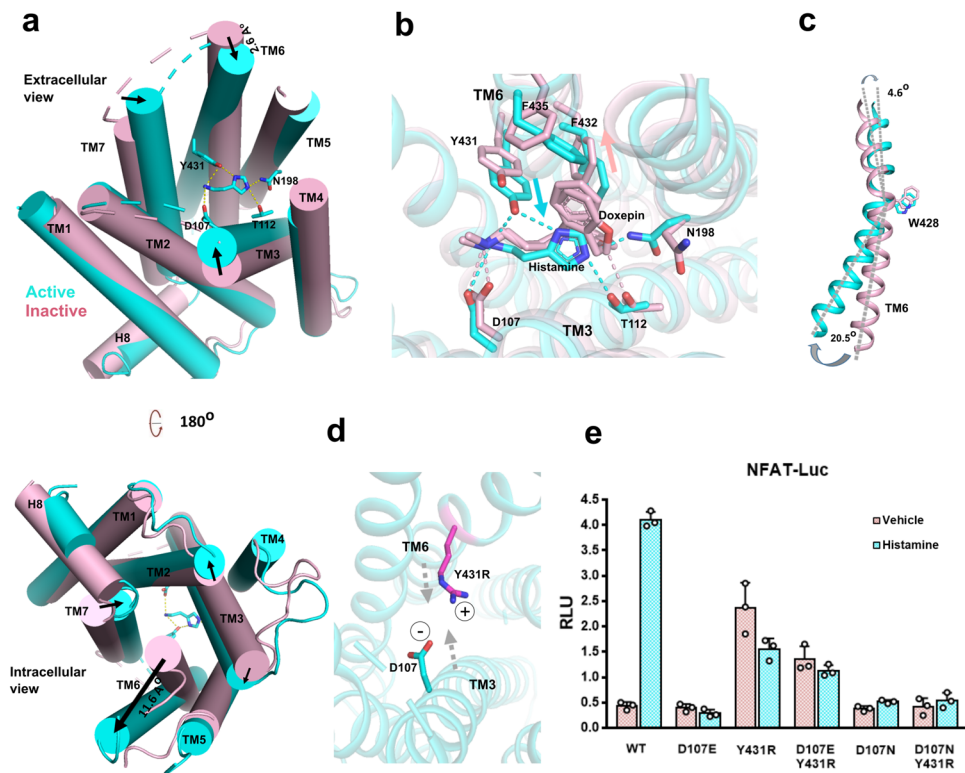


Fig. 3 Activation of H₁R by the binding of histamine. **a** A comparison of histamine-bound active H₁R and the inverse agonist doxepin-bound inactive H₁R (PDB 3RZE). The helices are shown in cylinders. Active receptor is shown in cyan and inactive receptor is shown in light pink. Up-panel is the extracellular side view and lower-panel is the intracellular side view. Arrows mark the movement of the designate part of receptor upon histamine binding. **b** A comparison of the agonist (histamine) binding pocket (cyan) with the inverse agonist (doxepin) binding pocket (light pink). The cyan arrow marks the movements of key residues on TM6 upon agonist (histamine) binding and the light pink arrow marks the movements of key residues on TM6 upon inverse agonist (doxepin) binding. **c** The movements of TM6. The W428^{6,48} severs as a pivot between the upside (extracellular) movement and the downside movement of TM6. **d** A simple model (for illustration only) of a designed salt bridge interaction between the Y431R mutation of TM6 and with the negative charge D107^{3,32} of TM3. **e** A NFAT-RE reporter assay of the Y431^{6,51} and D107^{3,32} mutations. Histamine, 10 μM; data are presented as mean values ± SD; *n* = 3 independent samples. RLU, relative luciferase unit.

Mutation of W428^{6,48} to A totally abolishes receptor activity (Supplementary Fig. 9b), indicating the importance of this residue in the switch of receptor activity. The DRY motif localizes on the lower part of TM3. In the inactive state, the Y125^{3,50} of DRY motif interacts with both A413^{6,33} and Q416^{6,36} of TM6 to lock receptor in an inactive conformation. Upon receptor activation, the interaction is broken as TM6 sways away from inside to outside (Supplementary Fig. 14d). The N464^{7,49} of the NPxxY motif on TM7 associates with D732^{5,0} in both active and inactive states, however, upon receptor activation, there is 8.2 Å displacement of Y468^{7,53} toward the center of the cavity when TM6 sways away, the aromatic ring of Y468^{7,53} also tilts about 40 degrees to form new contact with residue V118^{3,43}, L121^{3,46}, and R125^{3,50} of TM3 (Supplementary Fig. 14e). In the PIF motif, the most significant change is the side chain displacement of F424^{6,44} upon receptor activation, similar to the observation in the receptor activation of the HTR2A/mini-Gq complex¹⁷.

The engagement of G_q to H₁R. The engagement of G_q to H₁R is mainly maintained by key interaction from TM6, TM5, TM3, ICL2, and TM7-H8 kink region. The K412^{6,32} of TM6 makes a key interaction with the carboxy group of N357^{G.H5,24} of the αH5 (Fig. 4a). The side chain of N352^{G.H5,19} in αH5 forms a hydrogen bond with the backbone carbonyl of S128^{3,53} in TM3, while the last residue of αH5, Y356^{G.H5,23}, is blocked by the R125^{3,50} to prevent further intrusion (Fig. 4b). The ICL2/αN-β1 junction interaction has been reported in M1R/G₁₁ complex¹⁶, we also

observe a similar interaction in the H₁R/G_q complex but with a different pattern where the backbone carbonyl of Y135^{ICL2} forms a hydrogen bond with the αN-β1 junction. In TM7-H8 kink region, we observe a close contact of N474^{8,49} with the N357^{G.H5,24} of αH5 (Fig. 4a). Residue L133 in ICL2 is highly conserved in GPCR family and has been implicated play an important role in G_s and G_q coupling. Similar to the HTR2A/mini-G_q complex¹⁷, we found that the hydrophobic residue L133^{ICL2} intrudes into a hydrophobic “pocket” formed by L40, V199, F201, F341 and I348 of Gα_q (Supplementary Fig. 15). Mutation studies has suggested that this hydrophobic interaction play a crucial role in stabling the receptor/G_q complex¹⁷. Interestingly, we also observe a patch of interactions between the ICL1 and the Gβ subunit where the side chain of R56^{ICL1} forms a hydrogen bond with the backbone carbonyl of A309 of Gβ, and the H59^{ICL1} is in close contact with the negative charged D312 of Gβ (Fig. 4c).

The overall engagement of H₁R/G_q is similar to M1R/G₁₁ (Fig. 4d), however, distinct features were observed. Aligned with receptors, a comparison of M1R/G₁₁ with H₁R/G_q shows a clear difference in the orientation and position of G protein relative to receptor. The insertion of αH5 into H₁R is less deeper (about 1/2 helix) than the G₁₁ in M1R (Fig. 4e). Also the αH5 of G_q shows a 9.2 degree outward displacement in the H1R/G_q complex, we also observe the coordinated displacements on Gα RAS domain and Gβγ core domain (Fig. 4d). However, the largest observed displacement is the translational displacement of αN (9.5 Å as measured by the Ca of A7 between G_q and G₁₁) when aligned

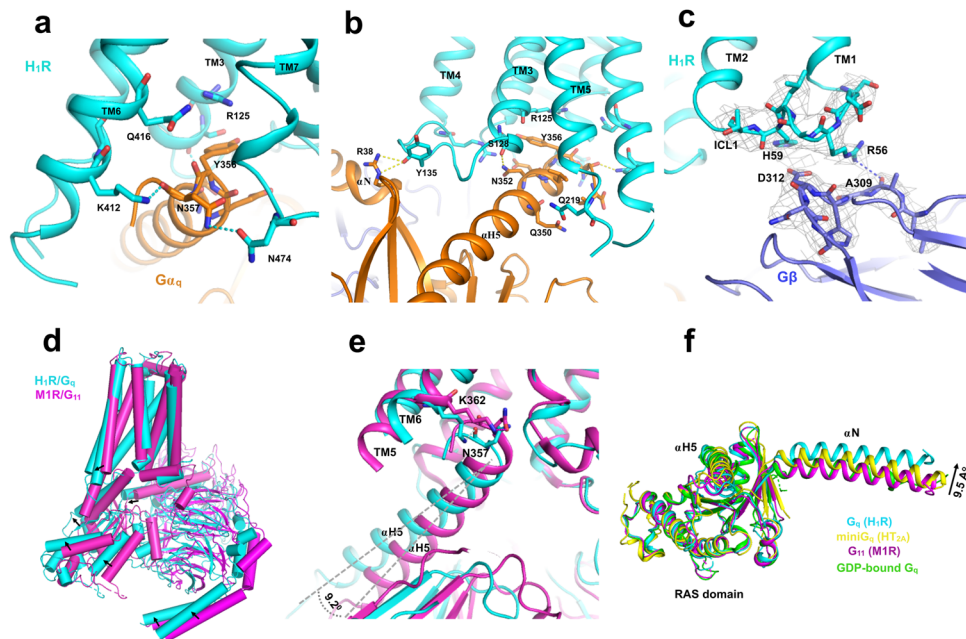


Fig. 4 The engagement G_q to H_1R . **a** The interaction between the receptor and the αH_5 , viewing from the TM6, TM7-H8 front angle. The receptor is colored in cyan and $G\alpha_q$ is colored in orange. **b** The interaction between the receptor and $G\alpha_q$, viewing from the TM5, TM3, and ICL2 front angle. **c** The ICL2/ $G\beta$ interaction. The receptor is colored in cyan and $G\beta$ is colored in slate. Density map of designated region is set to contour level of 3.0. **d** An overall comparison of the H_1R/G_q complex with the $M1R/G_{11}$ complex (PDB 6OIJ). **e** A comparison of the engagement of αH_5 to receptor between the H_1R/G_q complex with the $M1R/G_{11}$ complex. **f** A comparison of the αN displacements of $G_{q/11}$ in receptor engagement. $M1R/G_{11}$ (PDB 6OIJ), $HT2AR/mini-G_q$ (PDB 6WHA) and $GDP-bound G_q$ (PDB 3AH8).

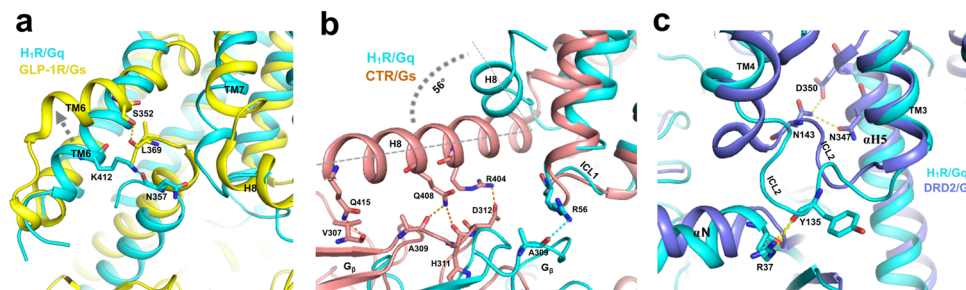


Fig. 5 Comparisons of G_q -coupled H_1R with G_s - and G_i -coupled receptors. **a** A comparison of the αH_5 engagement between $GLP-1R/G_s$ (PDB 5VAI) and the H_1R/G_q complex. The dashed arrow shows the additional outward displacement of the TM6 of $GLP-1R$. **b** A comparison of the $G\beta$ interactions between the CTR/G_s (PDB 5UZ7). **c** A comparison of the ICL2 interaction between the $DRD2/G_i$ (PDB 6VMS) and the H_1R/G_q complex.

with the core of RAS domain which seldom changes shape in receptor engagement (Fig. 4f). The αN of the H_1R/G_q complex shows a dramatic outward translational displacement compared to that of the $M1R/G_{11}$ and $HTR2A/mini-G_q$, as well as the $GDP-bound$ inactive G_q protein²⁷. While the interaction between ICL2 and αN - $\beta 1$ junction seems to be a common feature of the $G_{q/11}$ coupled receptor, H_1R use a different pattern to interact the junction in which the backbone carbonyl of $Y135^{ICL2}$ interacts with the side chain of $R38$ of G_q (Fig. 4b and Supplementary Fig. 16a), instead of the “head to toe” pattern observed in $M1R/G_{11}$ and $HTR2A/mini-G_q$ where the side chain of $R134^{ICL2}$ interact with the backbone carbonyl of $R37$, and the side chain of $R37$ interact with the backbone carbonyl of $R134^{ICL2}$ in the $M1R/G_{11}$ complex (for $HTR2A/mini-G_q$, the pattern is $R185^{ICL2}/R32$) (Supplementary Fig. 16). We speculate that the interaction difference may contribute to the large displacement of αN in the H_1R/G_q complex. In addition, we also find the $TM7$ - $H8$ kink/ αH_5 interaction might be a common feature for $G_{q/11}$ coupling receptors. In H_1R/G_q complex, the $N474^{8.49}$ interacts with the

$N357^{G.H5.24}$ of αH_5 (Fig. 4a and Supplementary Fig. 17). In $HTR2A/mini-G_q$ complex, the $N384^{8.47}$ interacts with $N244$ of the $mini-G_q$. Similarly in $M1R/G_{11}$, the $N422^{8.47}$ of $M1R$ is in a close contact with $E355^{G.H5.22}$ and $N357^{G.H5.24}$ of the αH_5 .

Comparison with GPCR- G_s and - G_i complexes. The structure of H_1R/G_q , $M1R/G_{11}$, and $HTR2A/mini-G_q$ complex, enable us to do a comparison of G_q -coupled with G_s -coupled and G_i -coupled receptor complex. Since G_s complex structures predominantly come from Class-B GPCR/ G_s complex, we first compare with the class B GPCR. It has been reported that the G_s family has the most pronounced outward displacement of $TM6$ in receptor activation. Compared to Glucagon-like peptide 1 receptor ($GLP-1R$)/ G_s complex²⁸, the $TM6$ of $GLP-1R$ shows a 6.0 Å more outward displacement than H_1R (Fig. 5a). Similar displacement of $TM6$ was observed on parathyroid hormone receptor-1 ($PTH1R$)²⁹ and calcitonin receptor (CTR)³⁰. We also noticed a different pattern of $TM6/\alpha H_5$ interaction. Instead of using the positive charged residue ($K412^{6.32}$ of H_1R and

K362^{6,32} of M1R) for α H5 interaction, the G_s-coupled receptor use serine or threonine (S352^{6,41} of GLP-1R and S409^{6,41} of PTH1R) for α H5 interaction (Fig. 5a). It has been reported that the G β subunit participates receptor interaction in class B GPCR/G_s complex^{22,28–30}, since we discovered an interaction between ICL1 and G β , we compared H₁R with class B GPCRs. We noticed a significant difference in the length and orientation of helix 8, the class B GPCRs have a much longer H8 than the G_q-coupling receptor (H₁R, M1R and HTR2A). Most notably, a H8 of G_s-coupled class B GPCR (CTR) shows a 56 degrees of tilt toward the G β subunit side, which explains the general observation of H8/G β interaction in this family (Fig. 5b). For instance, the Q415^{8,67}, Q408^{8,6} and R404^{8,56} of calcitonin receptor (CTR) make contact with V307, A309, and D312 of G β , respectively. On the other hand, H₁R use its ICL1 (R56^{ICL1}) to interact the G β subunit (A309) (Figs. 4c, 5b). The role of H8/G β interaction of the class B GPCR is generally believed to be related to receptor stability but not the receptor/G-protein coupling as mutations show little effect on the signaling^{28,30}. Consistent with this, mutation of R56^{ICL1} and H59^{ICL1} of the H₁R to alanine show no effect on the NFAT-RE reporter assay (Supplementary Fig. 18).

We then compare the class A G_s-coupled receptors with H₁R. There are only two class A GPCR/G_s complex structures (β 2-AR and β 1-AR) and two class A GPCR/mini-Gs (GPR52 and A_{2A}R) complex structures available. We first compare with Gs complexes. Similar to class B GPCR, the outward displacement of TM6 is more pronounced in β 2-AR and β 1-AR than H₁R (Supplementary Fig. 19a). The TM6/ α H5 interaction pattern is similar to class B GPCR, β 2-AR and β 1-AR use threonine (T274^{6,36} and T291^{6,36}, respectively) for α H5 interaction while H₁R use positive charged residue (K412^{6,32}) for α H5 interaction (Supplementary Fig. 19a). We also noticed a subtle difference of the TM3/ α H5 interaction. For instance, β 2-AR use both the last two residues (I135^{3,54}, T136^{3,55}) of TM3 to interact with the α H5 of G_s (Q384^{G.H5.5.16} and R380^{G.H5.5.12}) while the G_q-coupled receptor only use the second last residue of TM3 (S128^{3,53} of H₁R and S126^{3,53} of M1R) to interact the α H5 (N352^{G.H5.5.19} and Y356^{G.H5.5.23}) (Supplementary Fig. 19b). For the mini-Gs/Receptor complexes, a distinct feature is the TM5/ α H5 interaction (H233^{5,69} of GPR52 interact with Q384 of mini-G_s, and Q207^{5,63} of A_{2A}R interact with Q374 of mini-G_s) which has not been seen in H₁R or M1R (Supplementary Fig. 20).

Compared to the G_i-coupled receptors, the difference is much subtle, the most noticeable difference is the ICL2 interaction. The G_q-coupled receptors seem uniquely use the ICL2 to interact with the α N- β 1 junction of G α (Fig. 5c and Supplementary Fig. 16a), while the G_i-coupled receptors dominantly use the ICL2-TM4 junction to interact with the α H5. For instance, the D2 dopamine receptor (DRD2) use the N143^{ICL2} to interact with the D350^{G.H5.22} of the α H5 of G_i¹⁹ (Fig. 5c), while H₁R use the Y135^{ICL2} to interact with the R37 of the α N of G_q. Similarly, CB1²⁶ use P221^{ICL2}, CB2³¹ use K142^{ICL2} and μ -opioid receptor (μ OR)²⁰ use R179^{ICL2} to interact with the α H5 of G_i (Supplementary Fig. 21), and M1R use R134^{ICL2} to interact the R37 of the α N of G₁₁ (Supplementary Fig. 16a). On the G protein side, compared with G_s and G_i-coupled receptor complexes, the α N of H₁R/G_q complex displays the largest outward translational displacement (Supplementary Fig. 22) as seen in the G_q-coupled receptor complex (Fig. 4f). Mutations of key residues of H₁R (Y135A, K137A) that interacts with the α N- β 1 junction of G_q shows no severe effect on receptor activity on the NFAT-RE reporter assay (Supplementary Fig. 16b), suggesting that function of the large translational displacement of α N in H₁R/G_q complex may not directly relate to receptor coupling.

Discussion

In this study, we use the NanoBiT strategy to solved the structure of histamine-bound H₁R in complex with G_q via single-particle analysis of cryo-EM. To facilitate receptor expression and folding, we use a ICL3 truncation version of receptor (224-401) for structure study. It has been reported that the ICL3 contributes to the recognition and coupling of GPCRs with G_s, G_i, G_q and G_{12/13}^{13,14}, we therefore ask whether the ICL3 deletion will affect receptor activation. In a NFAT-RE reporter assay, the ICL3 deleted receptor responds ligand well, however, comparing the dose-response curve, the ICL3 truncation shows 10 folders higher of EC₅₀ than wild-type receptor (118.6 nM for wild type, 1651 nM for ICL3 truncation, Supplementary Fig. 23), suggesting that the ICL3 does contribute receptor activation and G_q coupling. We suspected that the flexible region of ICL3 may interact with α H5 and the Ras domain of the G α q that faces the receptor side, and those interactions may stabilize the receptor/G_q complex, the detail of those interaction is worthy of future investigation for a comprehensive understanding of G_q coupling. In summary, we have revealed the active conformation of H₁R in complex with G_q and presented a model of “squash to activate and expand to deactivate” for H₁R action. Our findings, including both the mechanistic insights and the featured observations of the G_q coupling will benefit both the understanding of G_q signaling and the rational design of novel antihistamines.

Methods

Constructs. The human H₁R gene was subcloned into the pFastBac plasmid with a HA-signal peptide sequence on its N-terminus and the LgBiT fused to its c-terminus followed by a Tobacco etch virus (TEV) cutting site and 2 fused maltose-binding proteins to facilitate protein expression and purification. A 12 amino sequence of GASGASGASGAS sequence was inserted between the receptor and LgBiT. The first 28 residues (residue 1-28) and the ICL3 loop (residue 224–401) of H₁R were chopped off to increase protein expression and folding. The HiBiT was fused to the c-terminus of human G β ₁ and cloned into pFastBac plasmid as described in the VIP1R paper²¹. The N-terminus (residue 1-32) of human G α _q was replaced by the N-terminus of G_i (residue 1–28) and subcloned into pFastBac plasmid. The wild-type human G γ ₂ was cloned into pFastBac plasmid. The scFv16 that encodes the single-chain variable fragment of mAb16 was subcloned into pFastBac plasmid.

Expression and purification of H₁R/G_q complex. Bacmid preparation and virus production were performed according to the Bac-to-Bac baculovirus system manual (Gibco, Invitrogen). For expression, the *Spodoptera frugiperda* (Sf9) cells at density of 2×10^6 cells per ml were co-infected with baculovirus encoding the H₁R-LgBiT-tev-2MBP, G α _{IN}, G β , G γ and scFv16 protein at a ratio of 1:100 (virus volume vs cells volume). Cells were harvest 48 h after infection. Cell pellets were resuspended in 20 mM Hepes buffer (pH 7.5), 150 mM NaCl, 10 mM MgCl₂, 20 mM KCl, 5 mM CaCl₂, and homogenized by douncing ~30 times. Apyase was added to the lysis at a final concentration of 0.5 mU/ml. To keep the complex stable, histamine was added at a final concentration of 100 μ M all through the purification procedure. The lysate was incubated at room temperature for 1 h with flipping. Then, n-dodecyl- β -D-maltoside (DDM) was added at the final concentration of 0.5% to solubilize the membrane at 4 °C for 2 h. Then the lysis was ultracentrifuged at 56,000g (45,000 rpm) at 4 °C for 40 min. The supernatant was collected and incubated with amylose column for 2 h. The amylose column was washed with a buffer of 25 mM Hepes (pH 7.5), 200 mM NaCl and 0.02% DDM, and 0.004% cholesteryl hemi-succinate (CHS), then eluted with the same buffer plus 10 mM maltose. The elution was concentrated and processed with home-made TEV for overnight at 4 °C. Then the digest was separated on a Superdex 200 Increase 10/300 GL (GE health science) gel infiltration column with a buffer of 25 mM Hepes (pH 7.5), 200 mM NaCl, and 0.1% digitonin (Biosynth). The peak corresponding to the H₁R/G_q complex was concentrated at about 10 mg/ml and snap frozen for later cryo-EM grid preparation.

Grid preparation and cryo-EM data collection. Three microliters of H₁R/G_q complex sample at ~10 mg/ml was applied to a glow-charged quantifoil R1.2/1.3 CuRh holey carbon grids (Quantifoil GmbH). The grids were vitrified in liquid ethane using Vitrobot Mark IV (Thermo Fisher Scientific) instrument in the setting of blot force of 10, blot time of 5 s, humidity of 100%, temperature of 6 °C. Grids were first screened on a FEI 200 kV Arctic transmission electron microscope (TEM) and grids with evenly distributed thin ice and promising grids were transferred to a FEI 300 kV Titan Krios TEM equipped with a Gatan Quantum

energy filter and a spherical corrector for data collection. Images were taken by a Gatan K3 direct electron detector at magnitude of 64,000, super-resolution counting model at pixel size of 0.54 Å, the energy filter slit was set to 20 eV. Each image was dose-fractionated in 32 frames using a total exposure time of 2.56 s at a dose rate of 1.56 e/Å²/s (total dose 50 e/Å²). All image stacks were collected by the EPU program of FEI, nominal defocus value varied from 1.2 to 2.0 μm.

Data processing. Raw movies at a size of 0.54 Å were binned once to generate a pixel size of 1.08 Å and then motion-corrected using MotionCor2³², followed by CTF estimation using CTFIND 4.1³³. Particles were picked from the micrographs using cryOLO³⁴. Then the picked particles (about 2.4 million) were extracted by RELION^{35,36} (version 3.1) and subjected to 2 rounds of reference-free 2D classification in RELION. About 650,000 particles were selected and the initial model was generated by cryoSPARC³⁷ ab initio. Then the model was used as reference in RELION 3D classification. Classes showed clear secondary structure features were select for a 3D refinement in RELION, followed by a Bayesian polishing³⁸ implemented in RELION. Then the polished particles were subject to one round of 2D classification to get rid of the irregular particles that may not contribute to the high resolution 3D reconstruction. Then, this was followed by a 3D refinement and a CTF refinement implemented in RELION. The CTF refined particles were subjected to a 3D classification with fine angular sampling which yields a promising class of 169,241 particles. Then the particles were transferred to cryoSPARC and followed a Non-uniform Refinement which yields a map of 3.64 Å based on the gold standard Fourier Shell Correlation (FSC) = 0.143 criterion. Later Phenix real_space-refinement show a resolution of 3.3 Å at 0.143. Local resolution estimations were performed using either RELION or cryoSPARC.

Model building. The crystal structures of human doxepin-bound H₁R¹⁰ (PDB 3RZE) and the G₁₁ protein complex from the MIR/G₁₁ (PDB 6OIJ)¹⁶ were used as initial models for model rebuilding and refinement against the electron microscopy map. All models were docked into the electron microscopy density map using UCSF Chimera³⁹. The resulting model was subjected to iterative manual adjustment using Coot⁴⁰, followed by a Rosetta cryoEM refinement⁴¹ at relax model and Phenix real_space refinement⁴². The model statistics were validated using MolProbity⁴³. Structural figures were prepared in UCSF Chimera³⁹ and PyMOL (<https://pymol.org/2/>). The statistics for data collection and refinement are included in Supplementary Table 1.

The NFAT-reporter assay. The nuclear factor of activated T-cells response element (NFAT-RE) reporter assay was performed according to the luciferase reporter assay for deciphering GPCR pathways paper²³ and Promega instruction. Briefly, AD293 cells were split into 24 well plates at a density of 40,000 per well. After one day of growth on 37 °C at 5% CO₂, cells (per well) were transfected with 100 ng of NFAT-RE-Luc, 10 ng of pcDNA3-H1R wild-type or mutations, 10 ng of pRGtkRenilla plasmids by X-tremeGENE HP (Roche) at a ratio 3:1 to DNA amount. 16 h after transfection, cells were induced by histamine at 10 μM or vehicle. Six hours after induction, cells were harvested and lysed by addition of 1× Passive Lysis Buffer (Promega), and luciferase activity was assessed by the Dual-Glo Luciferase system (Promega). Data were plotted as firefly luciferase activity normalized to Renilla luciferase activity in Relative Luciferase Units (RLU).

Structure and sequence comparison. The calculation of the pocket volume was done by the CASTp 3.0 server²⁴. Sequence alignment by the Clustal Omega⁴⁴ server and the representation of sequence alignment was generated using the ESPript⁴⁵ website (<http://esprict.ibcp.fr>). The generic residue numbering of GPCR is based on the GPCRdb⁴⁶ (<https://gpccdb.org/>).

Reporting summary. Further information on research design is available in the Nature Research Reporting Summary linked to this article.

Data availability

Data supporting the findings of this manuscript are available from the corresponding author upon reasonable request. A reporting summary for this article is available as a Supplementary Information file. Source data are provided with this paper. Structural data have been deposited with the PDB (accession number 7DFL), and maps have been deposited with the Electron Microscopy Data Bank (EMDB) with accession numbers EMD-30665.

Received: 2 December 2020; Accepted: 4 March 2021;

Published online: 07 April 2021

References

- Monczor, F. & Fernandez, N. Current knowledge and perspectives on histamine H1 and H2 receptor pharmacology: functional selectivity, receptor crosstalk, and repositioning of classic histaminergic ligands. *Mol. Pharm.* **90**, 640–648 (2016).
- Panula, P. et al. International Union of Basic and Clinical Pharmacology. XCVIII. Histamine receptors. *Pharm. Rev.* **67**, 601–655 (2015).
- Parsons, M. E. & Ganellin, C. R. Histamine and its receptors. *Br. J. Pharm.* **147**, S127–S135 (2006).
- Fung-Leung, W. P., Thurmond, R. L., Ling, P. & Karlsson, L. Histamine H4 receptor antagonists: the new antihistamines? *Curr. Opin. Investig. Drugs* **5**, 1174–1183 (2004).
- Leurs, R., Bakker, R. A., Timmerman, H. & de Esch, I. J. The histamine H3 receptor: from gene cloning to H3 receptor drugs. *Nat. Rev. Drug Discov.* **4**, 107–120 (2005).
- Yanai, K. & Tashiro, M. The physiological and pathophysiological roles of neuronal histamine: an insight from human positron emission tomography studies. *Pharm. Ther.* **113**, 1–15 (2007).
- Fein, M. N., Fischer, D. A., O’Keefe, A. W. & Sussman, G. L. CSACI position statement: Newer generation H1-antihistamines are safer than first-generation H1-antihistamines and should be the first-line antihistamines for the treatment of allergic rhinitis and urticaria. *Allergy Asthma Clin. Immunol.* **15**, 61 (2019).
- Naqvi, A. & Gerriets, V. Cetirizine. In *StatPearls [Internet]. Treasure Island (FL): StatPearls Publishing.* (2021).
- Tashiro, M. et al. Dose dependency of brain histamine H(1) receptor occupancy following oral administration of cetirizine hydrochloride measured using PET with [¹¹C]doxepin. *Hum. Psychopharmacol.* **24**, 540–548 (2009).
- Shimamura, T. et al. Structure of the human histamine H1 receptor complex with doxepin. *Nature* **475**, 65–70 (2011).
- Bjarnadottir, T. K. et al. Comprehensive repertoire and phylogenetic analysis of the G protein-coupled receptors in human and mouse. *Genomics* **88**, 263–273 (2006).
- Wettschreck, N. & Offermanns, S. Mammalian G proteins and their cell type specific functions. *Physiol. Rev.* **85**, 1159–1204 (2005).
- Inoue, A. et al. Illuminating G-protein-coupling selectivity of GPCRs. *Cell* **177**, 1933–1947.e1925 (2019).
- Flock, T. et al. Selectivity determinants of GPCR-G-protein binding. *Nature* **545**, 317–322 (2017).
- Harding, S. D. et al. The IUPHAR/BPS Guide to PHARMACOLOGY in 2018: updates and expansion to encompass the new guide to IMMUNOPHARMACOLOGY. *Nucleic Acids Res.* **46**, D1091–D1106 (2018).
- Maeda, S., Qu, Q., Robertson, M. J., Skiniotis, G. & Kobilka, B. K. Structures of the M1 and M2 muscarinic acetylcholine receptor/G-protein complexes. *Science* **364**, 552–557 (2019).
- Kim, K. et al. Structure of a hallucinogen-activated Gq-coupled 5-HT_{2A} serotonin receptor. *Cell* **182**, 1574–1588.e1519 (2020).
- Maeda, S. et al. Development of an antibody fragment that stabilizes GPCR/G-protein complexes. *Nat. Commun.* **9**, 3712 (2018).
- Yin, J. et al. Structure of a D2 dopamine receptor-G-protein complex in a lipid membrane. *Nature* **584**, 125–129 (2020).
- Koehl, A. et al. Structure of the micro-opioid receptor-Gi protein complex. *Nature* **558**, 547–552 (2018).
- Duan, J. et al. Cryo-EM structure of an activated VIP1 receptor-G protein complex revealed by a NanoBIT tethering strategy. *Nat. Commun.* **11**, 4121 (2020).
- Zhou, F. et al. Structural basis for activation of the growth hormone-releasing hormone receptor. *Nat. Commun.* **11**, 5205 (2020).
- Cheng, Z. et al. Luciferase reporter assay system for deciphering GPCR pathways. *Curr. Chem. Genomics* **4**, 84–91 (2010).
- Tian, W., Chen, C., Lei, X., Zhao, J. & Liang, J. CASTp 3.0: computed atlas of surface topography of proteins. *Nucleic Acids Res.* **46**, W363–W367 (2018).
- Rosenbaum, D. M. et al. Structure and function of an irreversible agonist-beta (2) adrenoceptor complex. *Nature* **469**, 236–240 (2011).
- Krishna Kumar, K. et al. Structure of a signaling cannabinoid receptor 1-G protein complex. *Cell* **176**, 448–458.e412 (2019).
- Nishimura, A. et al. Structural basis for the specific inhibition of heterotrimeric Gq protein by a small molecule. *Proc. Natl Acad. Sci. USA* **107**, 13666–13671 (2010).
- Zhang, Y. et al. Cryo-EM structure of the activated GLP-1 receptor in complex with a G protein. *Nature* **546**, 248–253 (2017).
- Zhao, L. H. et al. Structure and dynamics of the active human parathyroid hormone receptor-1. *Science* **364**, 148–153 (2019).
- Liang, Y. L. et al. Phase-plate cryo-EM structure of a class B GPCR-G-protein complex. *Nature* **546**, 118–123 (2017).
- Xing, C. et al. Cryo-EM structure of the human cannabinoid receptor CB2-Gi signaling complex. *Cell* **180**, 645–654.e613 (2020).
- Zheng, S. Q. et al. MotionCor2: anisotropic correction of beam-induced motion for improved cryo-electron microscopy. *Nat. Methods* **14**, 331–332 (2017).

33. Rohou, A. & Grigorieff, N. CTFFIND4: Fast and accurate defocus estimation from electron micrographs. *J. Struct. Biol.* **192**, 216–221 (2015).
34. Wagner, T. et al. SPHIRE-crYOLO is a fast and accurate fully automated particle picker for cryo-EM. *Commun. Biol.* **2**, 218 (2019).
35. Fernandez-Leiro, R. & Scheres, S. H. W. A pipeline approach to single-particle processing in RELION. *Acta Crystallogr. D. Struct. Biol.* **73**, 496–502 (2017).
36. Zivanov, J. et al. New tools for automated high-resolution cryo-EM structure determination in RELION-3. *eLife* **7**, <https://doi.org/10.7554/eLife.42166> (2018).
37. Punjani, A., Rubinstein, J. L., Fleet, D. J. & Brubaker, M. A. cryoSPARC: algorithms for rapid unsupervised cryo-EM structure determination. *Nat. Methods* **14**, 290–296 (2017).
38. Zivanov, J., Nakane, T. & Scheres, S. H. W. A Bayesian approach to beam-induced motion correction in cryo-EM single-particle analysis. *IUCr* **6**, 5–17 (2019).
39. Pettersen, E. F. et al. UCSF Chimera—a visualization system for exploratory research and analysis. *J. Comput. Chem.* **25**, 1605–1612 (2004).
40. Emsley, P. & Cowtan, K. Coot: model-building tools for molecular graphics. *Acta Crystallogr. D. Biol. Crystallogr.* **60**, 2126–2132 (2004).
41. Wang, R. Y. et al. Automated structure refinement of macromolecular assemblies from cryo-EM maps using Rosetta. *eLife* **5**, <https://doi.org/10.7554/eLife.17219> (2016).
42. Adams, P. D. et al. PHENIX: a comprehensive Python-based system for macromolecular structure solution. *Acta Crystallogr. D. Biol. Crystallogr.* **66**, 213–221 (2010).
43. Chen, V. B. et al. MolProbity: all-atom structure validation for macromolecular crystallography. *Acta Crystallogr. D. Biol. Crystallogr.* **66**, 12–21 (2010).
44. Madeira, F. et al. The EMBL-EBI search and sequence analysis tools APIs in 2019. *Nucleic Acids Res.* **47**, W636–W641 (2019).
45. Robert, X. & Gouet, P. Deciphering key features in protein structures with the new ENDscript server. *Nucleic Acids Res.* **42**, W320–W324 (2014).
46. Pandy-Szekeres, G. et al. GPCRdb in 2018: adding GPCR structure models and ligands. *Nucleic Acids Res.* **46**, D440–D446 (2018).

Acknowledgements

The authors thank the Cryo-EM facility of Harbin Institute of Technology and the Cryo-EM core of the Shuimu Bioscience (Beijing) for sample screening and data collection. We thank the Startup Funds of HIT Center for Life Science. We thank the National Natural Science Foundation of China (32070048 to Y.H.). We thank Dr. Zhiwei Huang for suggestion and support of this project.

Author contributions

Y.H. conceived the project and design the experiments. R.X. made the expression constructs, purified the proteins and assembled the complex. N.W. made mutation constructs and performed the functional assays. Z.X. purified the proteins and prepared the grids. Y.L. initial the project and made early constructs. J.S. made some mutation constructs. Y.H., A.Z., and C.G. collected the data. Y.H. solved the structure and wrote the manuscript. All authors contributed to data interpretation and preparation of the manuscript.

Competing interests

The authors declare no competing interests.

Additional information

Supplementary information The online version contains supplementary material available at <https://doi.org/10.1038/s41467-021-22427-2>.

Correspondence and requests for materials should be addressed to Y.H.

Peer review information *Nature Communications* thanks So Iwata and the other, anonymous, reviewer(s) for their contribution to the peer review of this work. Peer reviewer reports are available.

Reprints and permission information is available at <http://www.nature.com/reprints>

Publisher's note Springer Nature remains neutral with regard to jurisdictional claims in published maps and institutional affiliations.



Open Access This article is licensed under a Creative Commons Attribution 4.0 International License, which permits use, sharing, adaptation, distribution and reproduction in any medium or format, as long as you give appropriate credit to the original author(s) and the source, provide a link to the Creative Commons license, and indicate if changes were made. The images or other third party material in this article are included in the article's Creative Commons license, unless indicated otherwise in a credit line to the material. If material is not included in the article's Creative Commons license and your intended use is not permitted by statutory regulation or exceeds the permitted use, you will need to obtain permission directly from the copyright holder. To view a copy of this license, visit <http://creativecommons.org/licenses/by/4.0/>.

© The Author(s) 2021